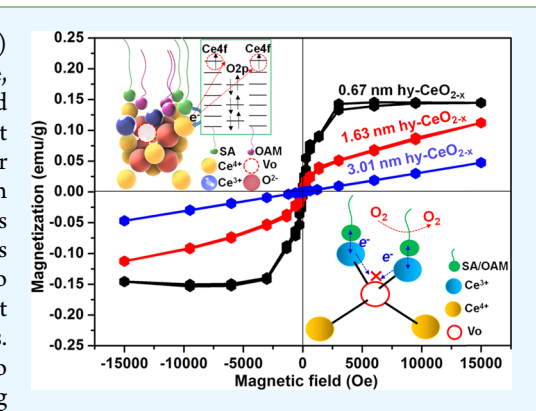


Enhanced Ferromagnetism from Organic-Cerium Oxide Hybrid **Ultrathin Nanosheets**

Guangyuan Yan, †,‡ Yizhan Wang,† Ziyi Zhang,† Jun Li,† Corey Carlos,† Lazarus N. German,† Chenyu Zhang, Jingyu Wang, Paul M. Voyles, and Xudong Wang*

Supporting Information

ABSTRACT: Room-temperature ferromagnetism in two-dimensional (2D) oxide materials is an intriguing phenomenon for spintronic applications. Here, we report significantly enhanced room-temperature ferromagnetism observed from ultrathin cerium oxide nanosheets hybridized with organic surfactant molecules. The hybrid nanosheets were synthesized by ionic layer epitaxy over a large area at the water-air interface. The nanosheets exhibited a saturation magnetization of 0.149 emu/g as their thickness reduced to 0.67 nm. This value was 5 times higher than that for CeO2 thin films and more than 20 times higher than that for CeO₂ nanoparticles. The magnetization was attributed to the high concentration (15.5%) of oxygen vacancies stabilized by surfactant hybridization as well as electron transfer between organic and oxide layers. This work brings an effective strategy of introducing strong ferromagnetism to functional oxide materials, which leads to a promising route toward exploring new physical properties in 2D hybrid nanomaterials.



KEYWORDS: ferromagnetism, organic-oxide hybrid, two-dimensional nanomaterials, ionic layer epitaxy, oxygen vacancies

INTRODUCTION

Since the discovery of graphene in 2004, two-dimensional (2D) nanomaterials have received considerable attention because of their unique physical and chemical properties originated from their ultrathin thickness and 2D morphology. 1,2 Very recently, 2D organic-inorganic hybrid nanomaterials, such as 2D metal-organic frameworks (MOFs) and 2D organic-inorganic hybrid perovskites (OIHPs), were created as a new member of the 2D nanomaterial family, enabling unique property coupling. MOFs are a crystalline porous compound in which the metal ions or clusters are linked by coordinating organic ligands to form bulky crystals. Due to various kinds of coordination modes between ligands and metal centers, MOFs offer impressive performance for catalytic, electrochemical, and sensing applications.³⁻⁵ Particularly, the 2D topological insulator MOF nanosheets exhibit unique quantum transport properties with potential applications in spintronics and quantum computing.^{6,7} 2D OIHPs represent a unique class of material that consists of alternating layers of insulating organic moieties and a semiconducting inorganic component, resembling a multiple quantum well structure. As a result, 2D OIHPs exhibit unique properties that are potentially useful for photonics applications.^{8,9} Additional organic-inorganic hybrid configurations were also reported, such as MoS₂/polyaniline nanowires with enhanced conductivity, thiophene-graphene heterostructure films with

enhanced volumetric capacitance for high-rate pseudocapacitors, and methyl-modified metal oxide nanotubes with enhanced hydrophobicity and organic molecule absorption for water decontamination. $^{10-12}$ These initial successes evidenced a promising strategy for creating new functional nanomaterials by hybridizing inorganic and organic molecules in 2D.

Recent research also showed that capping metal oxide with organic molecules could induce ferromagnetism by changing the electronic configuration through electron transfer between organic molecules and metal oxides. 13-15 For example, CeO₂ is a versatile functional oxide material that shows intriguing room-temperature ferromagnetism coupled with its conventional semiconducting and electrochemical properties. 16-18 However, the room-temperature ferromagnetism in CeO₂ nanocrystals was rather low. The typical value of saturation magnetization was only in the range from 0.001 to 0.014 emu/ g. 18 The weak ferromagnetism was associated with the low oxygen vacancy (Vo) concentration in CeO₂ (<5%), particularly at the crystal surfaces. 19-26 It is known that surface decoration of organic molecules could effectively stabilize the defects near crystal surfaces. 10,27-29 By reducing

Received: September 2, 2019 Accepted: November 5, 2019 Published: November 5, 2019

Department of Material Sciences and Engineering, University of Wisconsin-Madison, Madison, Wisconsin 53706, United States *Key Laboratory of Solidification Control and Digital Preparation Technology (Liaoning Province), School of Materials Science and Engineering, Dalian University of Technology, Dalian 116024, P. R. China

ACS Applied Materials & Interfaces

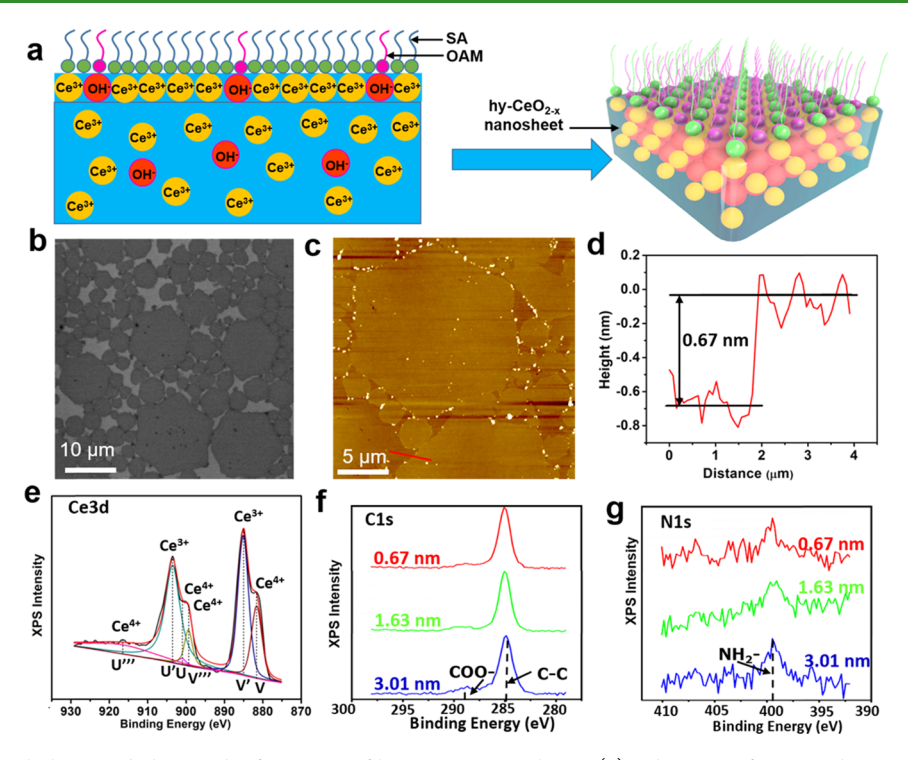


Figure 1. Synthesis, morphology, and elemental information of hy-CeO $_{2-x}$ nanosheets. (a) Schematic of ILE synthesis of hy-CeO $_{2-x}$ nanosheets. (b) SEM image of as-grown hy-CeO $_{2-x}$ nanosheets on a silicon substrate. (c) AFM topography scan of hy-CeO $_{2-x}$ nanosheets showing a uniform thickness. (d) Height profiles derived from the red line in (c). (e) XPS spectrum of characteristic X-ray peak of Ce $3d_{3/2}$ and $3d_{5/2}$ collected from the hy-CeO $_{2-x}$ nanosheets. (f) C 1s and (g) N 1s XPS spectra collected from the hy-CeO $_{2-x}$ nanosheets with thicknesses of 0.67, 1.63, and 3.01 nm.

the crystal thickness to the nanometer level where the surface effect becomes a dominating effect, we expect that the Vo concentration would be largely increased. Besides, certain organic molecules could donate electrons to metal ions and induce additional ferromagnetism to the oxides. Therefore, we hypothesize that a quasi-2D morphology of organic—oxide configuration might be able to offer significant improvement to the ferromagnetism in cerium oxides.

Herein, we report the development of ultrathin cerium oxide nanosheets hybridized with stearic acid (SA) and oleylamine (OAM) molecules. A significantly enhanced room-temperature ferromagnetism was recorded when the nanosheet thickness was reduced to 0.67 nm. The saturation magnetization was almost 5 times higher than that of CeO2 thin films and more than 20 times higher than those of CeO₂ nanoparticles. The magnetization was attributed to the hybridization of organic surfactants with the CeO_{2-x} nanosheets, which stabilized the high concentration of Vo and induced electron transfer between the organic surfactant layer and cerium oxide layer. Atomic layer deposition (ALD) coating and annealing in different atmospheres of nanosheets tuned the Vo concentration and surfactant bonding, which further confirmed the hybridization strategy to the emerging of strong magnetization in the CeO_{2-x} nanosheets.

■ RESULTS AND DISCUSSION

The CeO_{2-x} nanosheets were synthesized at the water—air interface by ionic layer epitaxy (ILE) under a monolayer of mixed surfactants of SA and OAM at a ratio of 9:1 (detailed synthesis conditions are included in Experimental Section). The mix-charge surfactant was recently discovered to be able to form a stable, flat, ordered template to direct the 2D growth

of crystalline oxides through ILE.³⁰ As revealed in Figure S1, the 9:1 ratio was experimentally determined as the optimal ratio for the formation of isolated hexagonal nanosheets with the most uniform thickness. In the weak alkaline environment, Ce³⁺ would form Ce(OH)₃, which would then be oxidized and dehydrated to CeO_{2-x} in the presence of trace oxygen in the solution.³¹ As a result, 100 min of reaction yielded ultrathin CeO_{2-x} nanosheets that were chemically bonded to the SA and OAM surfactants (hy-CeO_{2-x}), as shown in Figure 1a. Figure 1b shows a scanning electron microscopy (SEM) image of asreceived hy-CeO_{2-x} nanosheets supported on a SiO₂-coated Si substrate. The nanosheets nearly covered the entire surface of the substrate without any observable overlapping. All of the nanosheets had a hexagonal shape, while their size exhibited a bimodal distribution: large ones had a diagonal length of 11.5 \pm 0.8 μ m and small ones were 2.3 \pm 0.3 μ m. This bimodel distribution could be possibly attributed to the oriented attachment mechanism that was discovered in ILE processes, where smaller nuclei or nanosheets tend to merge into big nanosheets driven by the reduction of surface energy.³² Atomic force microscopy (AFM) topography image in Figure 1c revealed that the nanosheets had a very uniform thickness of 0.67 nm (Figure 1d) with a surface roughness of only 0.13 nm. The small bright dots observed near the nanosheet edges were particle byproducts formed in the bulk solution. The thickness of hy-CeO_{2-x} nanosheets could be controlled by the precursor concentration. As the concentration of Ce(NO₃)₃ increased from 0.2 to 1 mM and 1.5 mM, the thickness was raised from 1.63 to 3.01 nm and 4.92 nm, respectively (Figure S2). Meanwhile, as the thickness increased from 1.63 to 4.92 nm, large nanosheets became smaller and small ones disappeared. This was possibly because the thicker nanosheets were grown

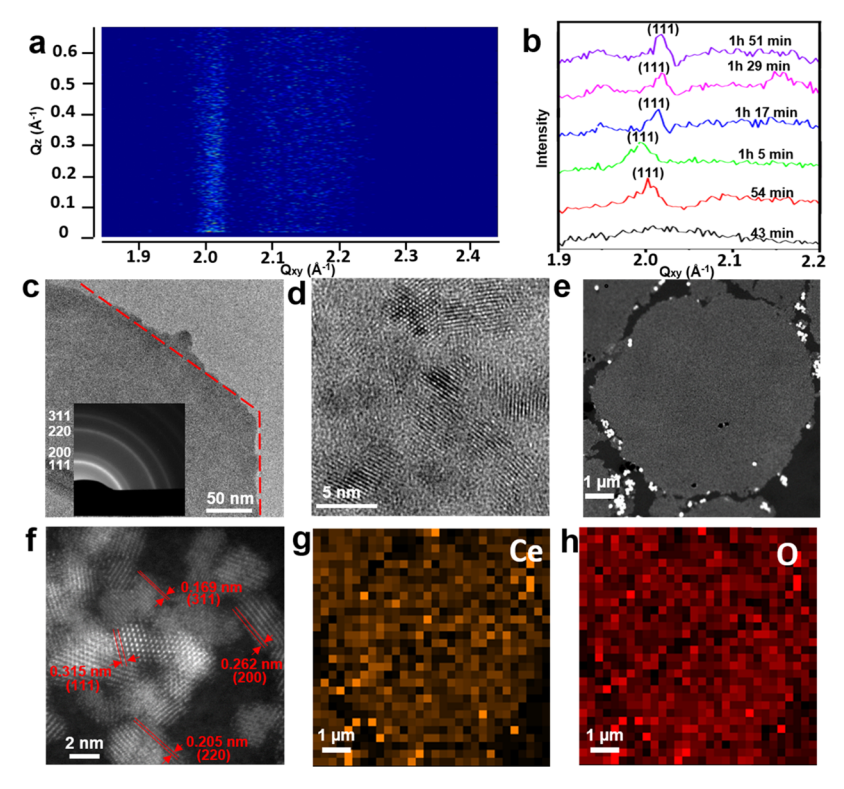


Figure 2. Structural characterization of hy-CeO_{2-x} nanosheets. (a) In situ grazing incidence X-ray diffraction (GIXRD) reciprocal space map of the hy-CeO_{2-x} nanosheets growing on the water surface. (b) In-plane GIXRD profiles of hy-CeO_{2-x} nanosheets at different reaction times. (c) TEM image taken from a corner of a large hy- CeO_{2-x} nanosheet. The inset is the corresponding SAED pattern of the nanosheet. (d) HRTEM image of the hy-CeO_{2-x} nanosheet in (c). (e) HAADF-STEM image of hy-CeO_{2-x} nanosheets after plasma treatment showing their morphology. (f) Highresolution HAADF-STEM image of the hy-CeO_{2-x} nanosheet revealing the assembly of nanoparticles in the nanosheets. (g, h) Large-area STEM-EDS elemental mapping of Ce (g) and O (h) from the nanosheet shown in (e).

under higher precursor concentrations, which were favorable for higher nucleation rates and thus higher nuclei concentrations. Therefore, the final size of each nanosheet would become smaller. 33,34 The higher nuclei concentration would reduce the spacing in between nanosheets and thus the small nanosheets would quickly transform into big nanosheets via rapid merging.

X-ray photoelectron spectroscopy (XPS) analysis was then carried out to investigate the oxidation state of Ce in the assynthesized hy-CeO_{2-x} nanosheets. Figure 1e shows the Ce 3d spectra, where the two typical sets of spin-orbit multiplets (U, U', U'' and V, V', V'') were observed, while U'' and V'' were too weak to appear. 35,36 These XPS peaks were attributed to tetravalent Ce⁴⁺ and trivalent Ce³⁺, where U (900.9 eV), U''' (916.5 eV), V (881.7 eV), and V"' (899.4 eV) correspond to Ce^{4+} and the doublet pair U' (903.5 eV) and V' (885.1 eV) correspond to Ce3+. This analysis revealed the coexistence of both Ce⁴⁺ and Ce³⁺. The stronger intensity of the U' and V' peaks suggests that the Ce3+ state was dominating in the assynthesized hy- CeO_{2-x} sample. Figure 1f and g compares the C 1s and N 1s XPS spectra of the hy- CeO_{2-x} nanosheets with different thicknesses. Two peaks at 284.8 and 289.0 eV were observed in the C 1s region of all three-thickness nanosheets, and they could be assigned to the alkyl chain (C-C) and carboxylate (COO⁻) carbon atoms, respectively, 37,38 evidencing the presence of SA surfactants. A single peak at 399.7 eV corresponding to N 1s confirmed the presence of OAM on the nanosheet surface. 39,40

In situ grazing incidence X-ray diffraction (GIXRD) was used to observe the 2D crystal evolution of the hy-CeO_{2-x} nanosheets. It was carried out directly at the water-air interface in grazing incidence (GI) in-plane mode with the incident beam nearly parallel to the liquid surface. Figure 2a shows a typical GIXRD reciprocal space map of the diffracted intensity along orthogonal Q_{xy} (horizontal) and Q_z (vertical) diffraction vector axes of the hy-CeO_{2-x} nanosheets. The scattered intensity for the reflection appeared as a scattering rod strictly parallel to the Q_z axis, which proved that the hy- CeO_{2-x} nanosheets were perfectly oriented with the 2D sheet plane aligned parallel to the liquid surface. Figure 2b shows the evolution of in-plane GIXRD patterns of the hy-CeO_{2-x} nanosheets as a function of growth time. The corresponding nanosheet morphology change is shown in Figure S3. At 43 min, no peaks could be observed when small round nanosheets appeared at the interface, indicating that the nanosheets were amorphous at the early stage. A diffraction peak at $Q_{xy} = 2.003$ \mathring{A}^{-1} first appeared from the 54 min sample, which is corresponding to the (111) facet of a face-centered cubic CeO₂, suggesting the beginning of crystallization as the hexagonal nanosheets started to form. From the 1 h 5 min sample, the (111) peak shifted slightly to lower Q_{xy} (1.993) $Å^{-1}$). This lattice expansion might be due to the appearance of more Ce³⁺ ions as a result of high Vo concentration. The (111) peak subsequently shifted back and stabilized at Q_{xy} (2.015) $\mathring{A}^{-1})$ as the growth time further progressed, corresponding to a lattice spacing of 0.312 nm. This lattice spacing was consistent with previously reported CeO₂ nanocrystals. ^{23,41,42} Meanwhile, the peak widths gradually decreased as the growth time increased, reflecting an increase of the lateral size of the crystalline domains.

ACS Applied Materials & Interfaces

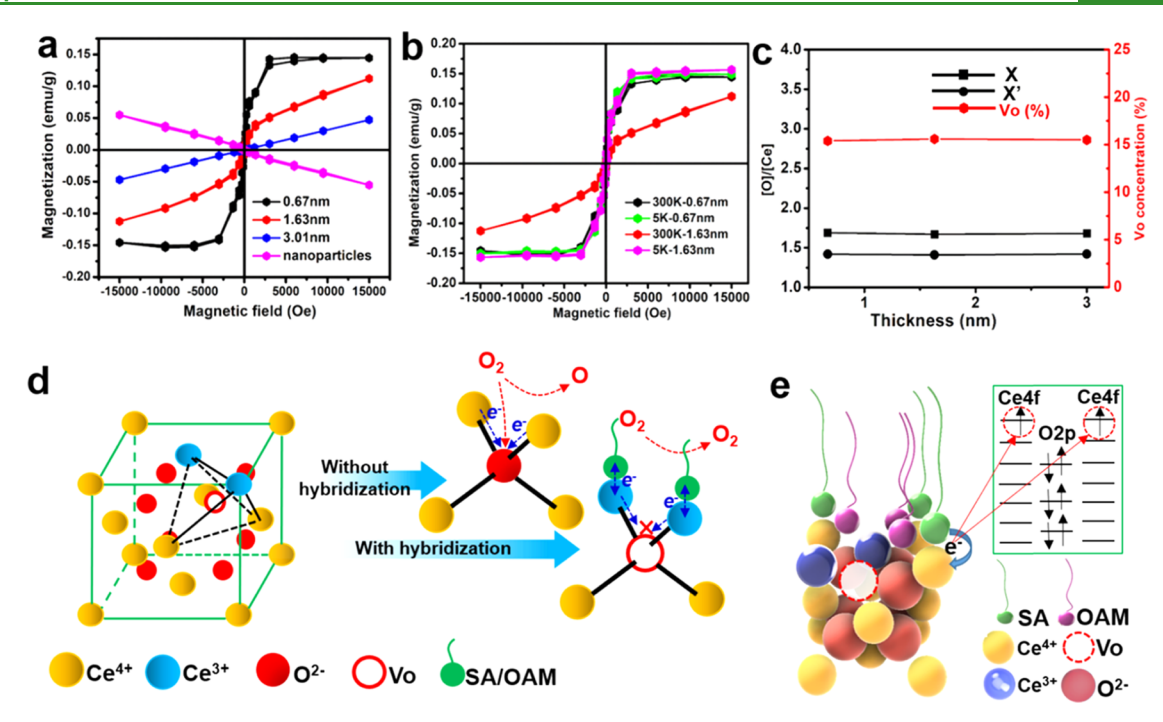


Figure 3. Magnetic properties of hy-CeO_{2-x} nanosheets. (a) M-H curves measured at 300 K from hy-CeO_{2-x} nanosheets with thicknesses of 0.67, 1.63, and 3.01 nm, respectively. The M-H curve from CeO_{2-x} nanoparticles is also shown for comparison. (b) Comparison of the M-H curves measured at 5 and 300 K for the 0.67 and 1.63 nm hy-CeO_{2-x} nanosheets. (c) CeO_{2-x} stoichiometry variations as a function of the nanosheet thickness calculated from the concentrations of Ce³⁺ and Ce⁴⁺ (black square), from the intensities of the O 1s and Ce 3d XPS peaks (black circle). Red hexagons represent the concentration of oxygen vacancy. (d) Schematic of how organic surfactant attachment would stabilize Vo in hy-CeO_{2-x} (e) Schematic illustration of a single unit cell of hy-CeO_{2-x} nanosheets with an oxygen vacancy and how it contributes to magnetization.

The crystal structure of the hy-CeO_{2-x} nanosheets was then characterized by transmission electron microscopy (TEM). Figure 2c shows a corner of a hexagonal nanosheet supported on a TEM grid. Although the nanosheet exhibited a roughly 120° corner as highlighted by the red line, the edges were wavy. The selected-area electron diffraction (SAED) pattern confirmed its polycrystalline structure (inset of Figure 2c), where the diffraction rings could be indexed to the (111), (200), (220), and (311) planes of CeO₂. High-resolution TEM (HRTEM) image in Figure 2d revealed that the nanosheet was composed of randomly oriented crystalline domains with sizes of 4-6 nm. Scanning transmission electron microscopy (STEM) was then conducted after treating the sample with 10 min plasma to remove surface organic coating. A high-angle annular dark-field STEM (HAADF-STEM) image showed that the nanosheets remained its original shape after the plasma treatment (Figure 2e). The highresolution image clearly illustrates that the crystalline domains were still 4-6 nm in sizes with randomly exposed facets (Figure 2f). Lattice spacings of the (111), (200), (220), and (311) planes were measured to be 0.315, 0.262, 0.205, and 0.169 nm, respectively, matching well with the SAED pattern. The clear lattice fringes and the unchanged size distribution of the crystalline domains after plasma treatment evidenced the good structural stability of the hy-CeO_{2-x} nanosheets. Energydispersive X-ray spectrum (EDS) elemental mapping reveals a uniform distribution of both Ce and O elements throughout the entire nanosheet (Figure 2g,h).

The magnetic property of the as-synthesized hy-CeO_{2-x} nanosheets with different thicknesses was examined by the magnetic hysteresis (M-H) loops measured at room temperature (Figure 3a). As a comparison, results from CeO_{2-x} nanoparticles synthesized under the same ILE condition

were also included. Meanwhile, the as-measured raw magnetic property data of 0.67, 1.63, and 3.01 nm hy-CeO_{2-x} nanosheets are included in Figure S4. They revealed that bare substrates had diamagnetic property and the ultrathin hy-CeO_{2-x} nanosheets exhibited an obvious enhancement in ferromagnetic property as their thickness reduced from 3.01 to 0.67 nm. After subtracting the diamagnetic signals from the substrate, Figure 3a clearly shows that the hy-CeO_{2-r} nanosheets with 3.01 nm thickness were paramagnetic. The 1.63 nm hy-CeO_{2-x} nanosheets showed ferromagnetism at low magnetic fields (-3000 to 3000 Oe), while paramagnetic contribution was still present at high magnetic fields. When the thickness was further reduced to 0.67 nm, the hy-CeO_{2-x} nanosheets became completely ferromagnetic with a saturation magnetization (Ms) of 0.149 emu/g. The Ms of the ultrathin hy-CeO_{2-x} nanosheets was almost 5 times larger than that of the reported CeO₂ thin films with a thickness of 40-50 nm, ²⁵ and 20 times larger than that of previously reported typical CeO_2 nanoparticles. Notably, CeO_{2-x} nanoparticles synthesized under the same ILE conditions only exhibited diamagnetic property. M-H curves of the 1.63 and 0.67 nm hy-CeO_{2-x} nanosheets measured at 5 K were compared to the room temperature results, as shown in Figure 3b. The magnetic behavior of 0.67 nm nanosheets was found nearly unchanged at 5 and 300 K. However, for the thicker 1.63 nm nanosheets, its saturation magnetization increased to 0.162 emu/g when the temperature reached 5 K.

Experimental and theoretical studies have shown that Vo could give rise to the room-temperature ferromagnetism in bulk and nanostructured CeO_{2-x} through the superexchange process between two reduced Ce^{3+} ions via $O^{2-}.^{20,21,43,44}$ The ordered magnetic moments within two Ce atoms and one O atom could induce spontaneous magnetization. 45-50 To

ACS Applied Materials & Interfaces

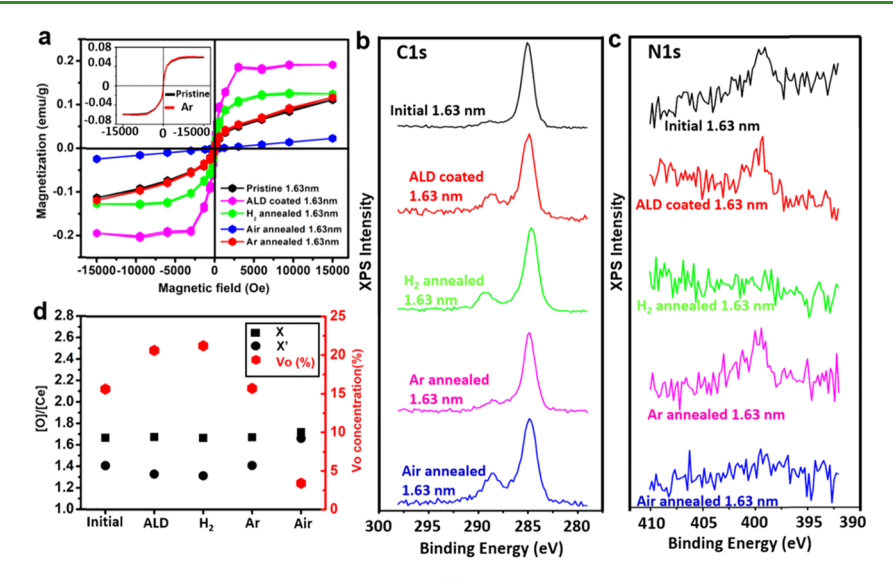


Figure 4. Understanding the ferromagnetism in hy-CeO_{2-x} nanosheets. (a) M-H curves measured at 300 K from 1.63 nm hy-CeO_{2-x} nanosheets as received, and after ALD coating, H2 annealing, air annealing, and Ar annealing. The inset shows the ferromagnetic component in the M-H curves from the pristine and Ar-annealed nanosheets after subtracting the paramagnetic component. (b) Comparison of the C 1s and (c) N 1s XPS peaks of the pristine 1.63 nm hy-CeO_{2-x} nanosheets and after being treated by ALD coating, H₂, Ar, and air annealing. (d) CeO_{2-x} stoichiometry variations in the 1.63 nm hy-CeO_{2-x} nanosheets after different treatments. Black squares are calculated from the concentrations of Ce³⁺ and Ce⁴⁺; black circles are calculated from the intensities of the O 1s and Ce 3d XPS peaks; and red hexagons represent the concentration of oxygen vacancy.

confirm and quantify the presence of Vo in the hy-CeO_{2-x} nanosheets, we compared the theoretical stoichiometry O content (X = [O]/[Ce]) with the actual stoichiometry O content (X' = O 1s/Ce 3d) based on the XPS spectra (Figure S5, calculation details are included in the Supporting Information, S2). X and X' were given and compared in Figure 3c. For all three-thickness samples, the actual stoichiometry O ratios (X') were generally smaller than the theoretical value (X), indicating oxygen deficiency in the hy-CeO_{2-x} nanosheets. It was also found that the Vo concentration was quite large, which remained at a constant value of 15.5% independent of the thickness variation. While such a high Vo concentration is generally unstable, the surfactant coating was believed to play a key role in stabilizing them. As shown in Figure 3d, when a Vo is formed in CeO₂, two electrons are left behind and localized at the 4f orbital of the two neighboring Ce atoms. Thus, the valency of these two Ce atoms was reduced to +3.20 At a large Vo concentration, these Ce3+ ions can easily be reoxidized to Ce4+ as the interaction between them would facilitate the removal of 4f electrons⁵¹ and thus makes Vo unstable. However, when organic molecules with negatively charged head groups are bonded to the surface, electrons transferred from the molecule could substitute the losing electrons and stabilize the Ce ions at +3. ^{16,27,37} This could protect the neighboring Vo from being oxidized and thus stabilize the large concentration of Vo.

Furthermore, previous studies also revealed that the Voinduced magnetic moment is strongly dependent on the location of the vacancy. Vo at the surface can induce nearly 50% higher magnetic moments than those induced by Vo in the bulk lattice.²¹ Despite having almost the same Vo concentration, the 0.67 nm-thick nanosheets had all of the ions and defects at the surface. As the thickness of one CeO₂ unit cell was 0.541 nm, 52 the 0.61 nm thickness was corresponding to a monolayer CeO₂ with organic surfactants. The 1.63 and 3.01 nm thicknesses were corresponding to three and five unit cells, respectively, where more Vo could be

distributed away from the surface. Therefore, the extremely higher surface-to-volume ratio resulted in a larger saturation magnetization in the 0.67 nm-thick hy-CeO_{2-x} nanosheets as compared to 1.63- and 3.01 nm-thick nanosheets. In addition, the organic surfactants layer can also induce ferromagnetism by electron transfer from the surfactant layer to the bonded Ce ions. $^{13,14,53-55}$ From the XPS spectra of the Ce $3d_{5/2}$ peaks (Figure S6), the peak position continuously shifted to lower blinding energy as the thickness increased from 0.67 to 1.63 nm and 3.01 nm, indicating that the inorganic CeO_{2-x} layer received electrons from the surfactants layer. 15,56 The superexchange process between two neighboring electron-receiving Ce ions and O 2p orbital could induce additional ordered magnetic moments, as shown in Figure 3e.

Therefore, we conclude that both Vo and electrons donated from the surfactant molecules contributed to the robust ferromagnetism observed in the hy-CeO_{2-x} nanosheets. This combined contribution was further validated experimentally. First, Vo concentration was tuned by introducing an ultrathin amorphous Al₂O₃ ALD coating. Due to the oxygen depletion from Al precursor bonding, the Vo concentration could be raised at the crystal/amorphous interface. M-H curves showed a significant increase of Ms from 0.059 to 0.19 emu/g after amorphous Al₂O₃ coating (Figure 4a). Accordingly, calculation of the Vo concentration from the XPS data (Table S2) confirmed that the Vo concentration was increased to 20.6% (Figure 4d). Meanwhile, stronger carboxylate (-COO-) peaks were observed in the ALD-coated sample (Figure 4b). This higher intensity could be attributed to the bonding between SA and CeO_{2-x} being shifted from monodentate to bidentate upon ALD coating. ^{37,39} Therefore, more electrons were transferred from the surfactant molecules to CeO_{2-x1} which further enhanced the ferromagnetism.

The as-received nanosheets were also annealed in different atmospheres to observe the magnetism change. Annealing the nanosheets in H₂ for 8 h raised the Vo concentration to 21.2% (Figure 4d). Similar stronger carboxylate XPS peaks as those shown in the ALD-coated samples were also observed. Accordingly, higher Ms of 0.13 emu/g was obtained from the H₂-annealed hy-CeO_{2-r} samples. The magnetization of nanosheets remained almost the same after Ar annealing because of the minimal change of Vo concentration (15.7%) and no obvious change of the -COO- and -NH2 bonding situation. However, air-annealed hy-CeO_{2-x} nanosheets became paramagnetic as a result of significantly reduced Vo concentration (3.2%) as well as the disappearance of the -NH₂ peak, which may be attributed to the decomposition of OAM at 250 °C. 39 All of these results confirmed that both Vo and surfactant bonding contributed to the enhanced magnetism of hy-CeO $_{2-x}$ nanosheets.

CONCLUSIONS

In conclusion, ultrathin 2D cerium oxide-based organicinorganic hybrid nanosheets with the thickness ranging from 0.67 to 3.01 nm were synthesized by ILE. Their magnetism was found dependent on the thickness. A significantly enhanced room-temperature ferromagnetism was observed when the thickness was reduced to 0.67 nm. Their saturation magnetization was almost 5-fold large than that reported previously for CeO2 thin films and more than 20 times higher than that reported previously for CeO₂ nanoparticles. The robust magnetization was attributed to the hybridization of the organic surfactant with the CeO_{2-x} nanosheets, which stabilized high concentration of Vo and enabled electron transfer between the organic surfactant layer and cerium oxide layer. ALD coating of the amorphous Al₂O₃ layer further increased the saturation magnetization to 0.19 emu/g by raising the Vo concentration from 15.5 to 20.6%. Annealing the nanosheets in different atmospheres (e.g., H₂, Ar, and air) further confirmed that the strong magnetization in hy-CeO_{2-x} nanosheets was attributed to the hybridization of the organic surfactant with the CeO_{2-x} nanosheets by tuning the Vo concentration and the binding situation. Our work highlights the hybridization of the organic surfactant with the CeO_{2-x} nanosheets, which can enhance the magnetization of cerium oxide nanosheets. This strategy opens up a promising avenue toward exploring new physical properties of novel 2D organicinorganic hybrid nanomaterials.

■ EXPERIMENTAL SECTION

Synthesis of hy-CeO_{2-x} Nanosheets. hy-CeO_{2-x} nanosheets were synthesized by ILE. Typically, 15 mL of aqueous solution containing 0.04 mM Ce(NO₃)₂ and 2 mM hexamethylenetetramine was prepared in a glass vial with a 4.5 cm² opening area. After standing the aqueous solution in air for 40 min, 6 µL of chloroform solution of mixed surfactants containing (~0.9 vol %) stearic acid (SA) solution and (~0.1 vol %) oleylamine (OAM) solution was spread on the water surface. The SA solution had a concentration of 1.8 mol/L. The OAM solution had a concentration of 1.8 mol/L and was mixed with hydrochloric acid to a concentration of 0.01 mol/L. This two-layer solution was exposed in atmosphere for 10 min to allow the chloroform to evaporate. Subsequently, the glass vial was screw-capped and placed in a 60 °C convection oven for 100 min for hy-CeO_{2-x} nanosheets to grow. The hy-CeO_{2-x} nanosheets were directly scooped onto a substrate for further characterization. Si substrates were used for SEM and AFM characterization. Au-coated Si substrates (50 nm) were used for XPS characterization. Holy carbon grids were used for TEM and STEM characterization. Sapphire substrates were used for magnetic measurement. After transferring, the nanosheets were dried naturally in air before characterization and property measurement. The ALD-coated sample was obtained by depositing 18-cycle Al₂O₃ on the hy-CeO_{2-x} nanosheets at 150 °C

(~0.1 nm per cycle). H₂, Ar, and Air annealing was performed in the corresponding atmosphere at 400 °C for 8 h, 200 °C for 2 h, and 300 °C for 2 h, respectively.

Material Characterization. The morphologies of the nanosheets were characterized by a Zeiss LEO 1530 field-emission scanning electron microscope. The atomic force microscopy tomography images were obtained using an XE-70 Park system. A Thermo Scientific K-alpha X-ray photoelectron spectroscopy (XPS) instrument with a 100 μ m spot size was used to obtain the XPS spectrum with the flood gun turned on during the measurements. In situ synchrotron grazing incidence X-ray diffraction (GIXRD) was performed by a liquid surface X-ray scattering instrument on beamline 15-ID-C (CHEMMATCARS Sectors 15) with an energy of 10.0000 keV and a wavelength of 1.23984 Å at the Advanced Photon Source (APS) in the Argonne National Laboratory. A FEI TF30 transmission electron microscope operated at 300 kV was used to study the crystal structure. High-angle annular dark-field scanning transmission electron microscopy (HAADF-STEM) imaging and STEM energydispersive X-ray spectrum (EDS) elemental mapping were conducted using a FEI Titan STEM with a probe aberration corrector at 200 kV. Superconducting quantum interference device (SQUID) magnetization measurements were carried out using a Quantum Design Magnetic Property Measurement System 3 (MPMS3) at DC mode with the magnetic field ranging from -15 000 to 15 000 Oe. The diamagnetic signals of substrates supporting the hy-CeO_{2-x} samples in the superconducting quantum interference device (SQUID) magnetometer were subtracted for all of the M-H curves. All of the magnetic hysteresis (M-H) curves were obtained by subtracting the signal of the bare substrate (diamagnetic signal) from the signals of hy-CeO_{2-x} samples on the substrate. The vertical coordinates of M-H curves were the magnetic moment differences between as-measured raw signals of hy-CeO_{2-x} on the substrate and the bare substrate divided by the mass of hy-CeO_{2-x} samples, while the magnetic field corresponded to the abscissa axis.

ASSOCIATED CONTENT

S Supporting Information

The Supporting Information is available free of charge on the ACS Publications website at DOI: 10.1021/acsami.9b15841.

Influences of the surfactant ratio, precursor concentration, and growth time on the morphology of hy-CeO_{2-x} nanosheets; as-measured raw M-H curves of hy-CeO_{2-x} nanosheets with the substrate; XPS spectrum of hy-CeO_{2-x} nanosheets with different thicknesses; and detailed calculation of Vo concentration (PDF)

AUTHOR INFORMATION

Corresponding Author

*E-mail: xudong@engr.wisc.edu.

ORCID ®

Guangyuan Yan: 0000-0002-1080-0138 Yizhan Wang: 0000-0003-0464-6610 Ziyi Zhang: 0000-0001-9102-8292 Jun Li: 0000-0002-7498-6736

Paul M. Voyles: 0000-0001-9438-4284 Xudong Wang: 0000-0002-9762-6792

Notes

The authors declare no competing financial interest.

ACKNOWLEDGMENTS

This work is supported by Army Research Office (ARO) under grant W911NF-16-1-0198 and the National Science Foundation under grant DMR-1709025. Electron microscopy experiments were supported by the Department of Energy Basic Energy Sciences under grant DE-FG02-08ER46547. Chem-MatCARS Sector 15 is supported by the National Science Foundation under grant NSF/CHE-1346572. This research used resources of the Advanced Photon Source, a U.S. Department of Energy (DOE) Office of Science User Facility operated for the DOE Office of Science by Argonne National Laboratory under contract DE-AC02-06CH11357. The Quantum Design MPMS3 magnetometer was supported by the Department of Chemistry, University of Wisconsin-Madison. This work is also supported by China Scholarship Council.

REFERENCES

- (1) Novoselov, K. S.; Geim, A. K.; Morozov, S. V.; Jiang, D.; Zhang, Y.; Dubonos, S. V.; Grigorieva, I. V.; Firsov, A. A. Electric Field Effect in Atomically Thin Carbon Films. Science 2004, 306, 666-669.
- (2) Tan, C. L.; Cao, X. H.; Wu, X. J.; He, O. Y.; Yang, J.; Zhang, X.; Chen, J. Z.; Zhao, W.; Han, S. K.; Nam, G. H.; Sindoro, M.; Zhang, H. Recent Advances in Ultrathin Two-Dimensional Nanomaterials. Chem. Rev. 2017, 117, 6225-6331.
- (3) Zhao, M. T.; Wang, Y. X.; Ma, Q. L.; Huang, Y.; Zhang, X.; Ping, J. F.; Zhang, Z. C.; Lu, Q. P.; Yu, Y. F.; Xu, H.; Zhao, Y. L.; Zhang, H. Ultrathin 2D Metal-Organic Framework Nanosheets. Adv. Mater. 2015, 27, 7372-7378.
- (4) Zhang, T.; Lin, W. B. Metal-organic Frameworks for Artificial Photosynthesis and Photocatalysis. Chem. Soc. Rev. 2014, 43, 5982-
- (5) Rodenas, T.; Luz, I.; Prieto, G.; Seoane, B.; Miro, H.; Corma, A.; Kapteijn, F.; i Xamena, F. X. L.; Gascon, J. Metal-organic Framework Nanosheets in Polymer Composite Materials for Gas Separation. Nat. Mater. 2015, 14, 48-55.
- (6) Wang, Z. F.; Su, N.; Liu, F. Prediction of a Two-Dimensional Organic Topological Insulator. Nano Lett. 2013, 13, 2842-2845.
- (7) Kambe, T.; Sakamoto, R.; Kusamoto, T.; Pal, T.; Fukui, N.; Hoshiko, K.; Shimojima, T.; Wang, Z.; Hirahara, T.; Ishizaka, K.; Hasegawa, S.; Liu, F.; Nishihara, H. Redox Control and High Conductivity of Nickel Bis (dithiolene) Complex π -Nanosheet: A Potential Organic Two-Dimensional Topological Insulator. J. Am. Chem. Soc. 2014, 136, 14357-14360.
- (8) Zhang, Q.; Chu, L. Q.; Zhou, F.; Ji, W.; Eda, G. Excitonic Properties of Chemically Synthesized 2D Organic-Inorganic Hybrid Perovskite Nanosheets. Adv. Mater. 2018, 30, No. 1704055.
- (9) Saparov, B.; Mitzi, D. B. Organic-inorganic Perovskites: Structural Versatility for Functional Materials Design. Chem. Rev. 2016, 116, 4558-4596.
- (10) Yang, L. C.; Wang, S. N.; Mao, J. J.; Deng, J. W.; Gao, Q. S.; Tang, Y.; Schmidt, O. G. Hierarchical MoS2/Polyaniline Nanowires with Excellent Electrochemical Performance for Lithium-Ion Batteries. Adv. Mater. 2013, 25, 1180-1184.
- (11) Wu, Z. S.; Zheng, Y. J.; Zheng, S. H.; Wang, S.; Sun, C. L.; Parvez, K.; Ikeda, T.; Bao, X. H.; Müllen, K.; Feng, X. L. Stacked-layer Heterostructure Films of 2D Thiophene Nanosheets and Graphene for High-rate all-solid-state Pseudocapacitors with Enhanced Volumetric Capacitance. Adv. Mater. 2017, 29, No. 1602960.
- (12) Amara, M. S.; Paineau, E.; Rouzière, S.; Guiose, B.; Krapf, M. E. M.; Taché, O.; Launois, P.; Thill, A. Hybrid, Tunable-diameter, Metal Oxide Nanotubes for Trapping of Organic molecules. Chem. Mater. **2015**, 27, 1488–1494.
- (13) Crespo, P.; Litran, R.; Multigner, M.; de la Fuente, J. M.; Lopez, J. C. S.; Garcia, M. A.; Cartes, C. L.; Hernando, A.; Penades, S.; Fernandez, A. Permanent Magnetism, Magnetic Anisotropy, and Hysteresis of Thiol-capped Gold Nanoparticles. Phys. Rev. Lett. 2004, 93, No. 087204.
- (14) Garcia, M. A.; Merino, J. M.; Pinel, E. F.; Quesada, A.; de la Venta, J.; Gonza'lez, M. L. R.; Castro, G. R.; Crespo, P.; Llopis, J.; Gonza'lez-Calbet, J. M.; Hernando, A. Magnetic Properties of ZnO Nanoparticles. Nano Lett. 2007, 7, 1489-1494.

- (15) Zhang, J. H.; Xiong, S. J.; Wu, X. L.; Thurber, A.; Jones, M.; Gu, M.; Pan, Z. D.; Tenne, D. A.; Hanna, C. B.; Du, Y. W.; Punnoose, A. Fluctuant Magnetism in Metal Oxide Nanocrystals Capped with Surfactants. Phys. Rev. B 2013, 88, No. 085437.
- (16) Paier, J.; Penschke, C.; Sauer, J. Oxygen Defects and Surface Chemistry of Ceria: Quantum Chemical Studies Compared to Experiment. Chem. Rev. 2013, 113, 3949-3958.
- (17) Arul, N. S.; Mangalaraj, D.; Ramachandran, R.; Grace, A. N.; Han, J. I. Fabrication of CeO₂/Fe₂O₃ Composite Nanospindles for Enhanced Visible Light Driven Photocatalysts and Supercapacitor Electrodes. J. Mater. Chem. A 2015, 3, 15248-15258.
- (18) Ackland, K.; Coey, J. M. D. Room Temperature Magnetism in CeO₂-A Review. Phys. Rep. 2018, 746, 1-39.
- (19) Sundaresan, A.; Bhargavi, R.; Rangarajan, N.; Siddesh, U.; Rao, C. N. R. Ferromagnetism as a Universal Feature of Nanoparticles of the otherwise Nonmagnetic Oxides. Phys. Rev. B 2006, 74, No. 161306.
- (20) Han, X. P.; Lee, J. C.; Yoo, H. I. Oxygen-vacancy-induced Ferromagnetism in CeO₂ from First Principle. Phys. Rev. B 2009, 79, No. 100403.
- (21) Ge, M. Y.; Wang, H.; Liu, E. Z.; Liu, J. F.; Jiang, J. Z.; Li, Y. K.; Xu, Z. A.; Li, H. Y. On the Origin of Ferromagnetism in CeO₂ Nanocubes. Appl. Phys. Lett. 2008, 93, No. 062505.
- (22) Bernardi, M. I. B.; Mesquita, A.; Béron, F.; Pirota, K. R.; de Zevallos, A. O.; Doriguetto, A. C.; de Carvalho, H. B. The Role of Oxygen Vacancies and Their Location in the Magnetic Properties of $Ce_{1-x}Cu_xO_{2-\delta}$ nanorods. Phys. Chem. Chem. Phys. **2015**, 17, 3072–
- (23) Li, M. J.; Ge, S. H.; Qiao, W.; Zhang, L.; Zuo, Y. L.; Yan, S. M. Relationship between the Surface Chemical States and Magnetic Properties of CeO₂ Nanoparticles. Appl. Phys. Lett. 2009, 94, No. 152511.
- (24) Chen, S. Y.; Tsai, C. H.; Huang, M. Z.; Yan, D. C.; Huang, T. W.; Gloter, A.; Chen, C. L.; Lin, H. J.; Chen, C. T.; Dong, C. L. Concentration Dependence of Oxygen Vacancy on the Magnetism of CeO₂ Nanoparticles. J. Phys. Chem. C 2012, 116, 8707-8713.
- (25) Meng, F. M.; Zhang, C.; Fan, Z. H.; Gong, J. F.; Li, A. X.; Ding, Z. L.; Tan, H. B.; Zhang, M.; Wu, G. F. Hydrothermal Synthesis of Hexagonal CeO2 Nanosheets and their Room Temperature Ferromagnetism. J. Alloys Compd. 2015, 647, 1013-1021.
- (26) Aidhy, D. S.; Liu, B.; Zhang, Y. W.; Weber, W. Chemical Expansion Affected Oxygen Vacancy Stability in Different Oxide Structures from First Principles Calculations. J. Comput. Mater. Sci. 2015, 99, 298-305.
- (27) Wu, Y. Q.; Lu, G. X. The Roles of Density-tunable Surface Oxygen Vacancy over Bouquet-like Bi₂O₃ in Enhancing Photocatalytic Activity. Phys. Chem. Chem. Phys. 2014, 16, 4165-4175.
- (28) Liu, H.; Luo, M.; Hu, J.; Zhou, T.; Chen, R.; Li, J. β -Bi₂O₃ and Er³⁺ Doped β -Bi₂O₃ Single Crystalline Nanosheets with Exposed Reactive {0 0 1} Facets and Enhanced Photocatalytic Performance. Appl. Catal., B 2013, 140-141, 141-150.
- (29) Xie, J. F.; Zhang, H.; Li, S.; Wang, R. X.; Sun, X.; Zhou, M.; Zhou, J. F.; Lou, X. W.; Xie, Y. Defect-rich MoS₂ Ultrathin Nanosheets with Additional Active Edge Sites for Enhanced Electrocatalytic Hydrogen Evolution. Adv. Mater. 2013, 25, 5807-
- (30) Wang, Y. Z.; Shi, Y. Q.; Zhang, Z. Y.; Carlos, C.; Zhang, C. Y.; Bhawnani, K.; Li, J.; Wang, J. Y.; Voyles, P. M.; Szlufarska, L.; Wang, X. D. Bioinspired Synthesis of Quasi-Two-Dimensional Monocrystalline Oxide. Chem. Mater. 2019, 31, 9040-9048.
- (31) Xu, C.; Wang, X.; Zhu, J. W. Graphene-metal Particle Nanocomposites. J. Phys. Chem. C 2008, 112, 19841-19845.
- (32) Wang, F.; Seo, J. H.; Luo, G.; Starr, M. B.; Li, Z.; Geng, D.; Yin, X.; Wang, S.; Fraser, D. G.; Morgan, D.; Ma, Z.; Wang, X. Nanometre-thick Single-crystalline Nanosheets Grown at the Water-air Interface. Nat. Commun. 2016, 7, No. 10444.
- (33) Loginov, E.; Gomez, L. F.; Chiang, N.; Halder, A.; Guggemos, N.; Kresin, V. V.; Vilesov, A. F. Photoabsorption of Ag-N (N similar to 6-6000) Nanoclusters Formed in Helium Droplets: Transition

- from Compact to Multicenter Aggregation. Phys. Rev. Lett. 2011, 106, No. 233401.
- (34) Boatwright, A.; Feng, C.; Spence, D.; Latimer, E.; Binns, C.; Ellis, A. M.; Yang, S. Helium droplets: a new route to nanoparticles. *Faraday Discuss.* **2013**, *162*, 113–124.
- (35) He, H.; Dai, H. X.; Au, C. T. Defective Structure, Oxygen Mobility, Oxygen Storage Capacity, and Redox Properties of RE-based (RE = Ce, Pr) Solid Solutions. *Catal. Today* **2004**, *90*, 245–254.
- (36) Patsalas, P.; Logothetidis, S. Structure-dependent Electronic Properties of Nanocrystalline Cerium Oxide Films. *Phys. Rev. B* **2003**, *68*, No. 035104.
- (37) Lim, M. S.; Feng, K.; Chen, X. Q.; Wu, N. Q.; Raman, A.; Nightingale, J.; Gawalt, E. S.; Korakakis, D.; Hornak, L. A.; Timperman, A. T. Adsorption and desorption of stearic acid self-assembled monolayers on aluminum oxide. *Langmuir* **2007**, 23, 2444—2452
- (38) Bournel, F.; Laffon, C.; Parent, P.; Tourillon, G. Adsorption of Acrylic Acid on Aluminium at 300 K: A Multi-spectroscopic Study. *Surf. Sci.* **1996**, 352–354, 228–231.
- (39) Wilson, D.; Langell, M. A. XPS Analysis of Oleylamine/oleic Acid Capped Fe₃O₄ Nanoparticles as a Function of Temperature. *Appl. Surf. Sci.* **2014**, *303*, 6–13.
- (40) Aslam, M.; Schultz, E. A.; Sun, T.; Meade, T.; Dravid, V. P. Synthesis of Amine-stabilized Aqueous Colloidal Iron Oxide Nanoparticles. *Cryst. Growth Des.* **2007**, *7*, 471–475.
- (41) Wu, L. J.; Weismann, H. J.; Moodenbaugh, A. R.; Klie, R. F.; Zhu, Y. M.; Welch, D. O.; Suenaga, M. Oxidation State and Lattice Expansion of CeO_{2-x} Nanoparticles as a Function of Particle Size. *Phys. Rev. B* **2004**, *69*, No. 125415.
- (42) Kumar, P. S. M.; Thiripuranthagan, S.; Imai, T.; Kumar, G.; Pugazhendhi, A.; Vijayan, R.; Esparza, S. R.; Abe, H.; Krishnan, S. K. Pt Nanoparticles Supported on Mesoporous CeO2 Nanostructures Obtained through Green Approach for Efficient Catalytic Performance toward Ethanol Electro-oxidation. ACS Sustainable Chem. Eng. 2017, 5, 11290–11299.
- (43) Venkatesan, M.; Fitzgerald, C. B.; Coey, J. M. D. Thin Films: Unexpected Magnetism in A Dielectric Oxide. *Nature* **2004**, *430*, 630.
- (44) Coey, J. M. D.; Venkatesan, M.; Stamenov, P.; Fitzgerald, C. B.; Dorneles, L. S. Magnetism in Hafnium Dioxide. *Phys. Rev. B* **2005**, *72*, No. 024450.
- (45) Weiss, P. L'hypothèse Du Champ Moléculaire et La Propriété Ferromagnétique. J. Phys. Theor. Appl. 1907, 6, 661–690.
- (46) Stone, E. C. Collective Electron Ferronmagnetism. *Proc. R. Soc. London, Ser. A* 1938, 165, 372–414.
- (47) Stone, E. C. Collective Electron Ferromagnetism II. Energy and Specific Heat. *Proc. R. Soc. London, Ser. A* **1939**, *169*, 339–371.
- (48) Ma'Mari, F. A.; Moorsom, T.; Teobaldi, G.; Deacon, W.; Prokscha, T.; Luetkens, H.; Lee, S.; Sterbinsky, G. E.; Arena, D. A.; MacLaren, D. A.; Flokstra, M.; Ali, M.; Wheeler, M. C.; Burnell, G.; Hickey, B. J.; Cespedes, O. Beating the Stoner Criterion Using Molecular Interfaces. *Nature* **2015**, 524, 69–73.
- (49) Fernandes, V.; Mossanek, R. J. O.; Schio, P.; Klein, J. J.; de Oliveira, A. J. A.; Ortiz, W. A.; Mattoso, N.; Varalda, J.; Schreiner, W. H.; Abbate, M.; Mosca, D. H. Dilute-defect Magnetism: Origin of Magnetism in Nanocrystalline CeO₂. *Phys. Rev. B* **2009**, *80*, No. 035202.
- (50) Fernandes, V.; Schio, P.; de Oliveira, A. J. A.; Ortiz, W. A.; Fichtner, P.; Amaral, L.; Graff, I. L.; Varalda, J.; Mattoso, N.; Schreiner, W. H.; Mosca, D. H. Ferromagnetism induced by oxygen and cerium vacancies above the percolation limit in CeO₂. *J. Phys.: Condens. Matter* **2010**, *22*, No. 216004.
- (51) Zhang, C. J.; Michaelides, A.; King, D. A.; Jenkins, S. J. Oxygen Vacancy Clusters on Ceria: Decisive Role of Cerium f Electrons. *Phys. Rev. B* **2009**, *79*, No. 075433.
- (52) Vodungbo, B.; Zheng, Y.; Vidal, F.; Demaille, D.; Etgens, V. H.; Mosca, D. H. Room Temperature Ferromagnetism of Co Doped CeO_{2-δ} Diluted Magnetic Oxide: Effect of Oxygen and Anisotropy. *Appl. Phys. Lett.* **2007**, *90*, No. 062510.

- (53) Carmeli, I.; Leitus, G.; Naaman, R.; Reich, S.; Vager, Z. Magnetism Induced by the Organization of Self-assembled Monolayers. *J. Chem. Phys.* **2003**, *118*, 10372.
- (54) Hernando, A.; Crespo, P.; García, M. A.; Pinel, E. F.; de la Venta, J.; Fernández, A.; Penadés, S. Giant Magnetic Anisotropy at the Nanoscale: Overcoming the Superparamagnetic Limit. *Phys. Rev. B* **2006**, *74*, No. 052403.
- (55) Zhang, P.; Sham, T. K. X-ray Studies of the Structure and Electronic Behavior of Alkanethiolate-capped Gold Nanoparticles: the Interplay of Size and Surface Effects. *Phys. Rev. Lett.* **2003**, *90*, No. 245502.
- (56) Uhlrich, J. J.; Franking, R.; Hamers, R. J.; Kuech, T. F. Sulfide Treatment of ZnO Single Crystals and Nanorods and the Effect on P3HT-ZnO Photovoltaic Device Properties. *J. Phys. Chem. C* **2009**, 113, 21147–21154.